PHYSICAL REVIEW C **109**, 015203 (2024)

Analysis of the $\Xi(1620)$ resonance and $\bar{K}\Lambda$ scattering length with a chiral unitary approach

Takuma Nishibuchi[*] and Tetsuo Hyodo[†]
Department of Physics, Tokyo Metropolitan University, Hachioji 192-0397, Japan

(Received 6 June 2023; accepted 8 December 2023; published 22 January 2024)

We study the $\Xi(1620)$ resonance near the $\bar{K}\Lambda$ threshold in the light of recent experimental constraints. The Belle Collaboration have found a resonance peak of $\Xi(1620)$ slightly below the $\bar{K}^0\Lambda$ threshold in the $\pi^+\Xi^-$ invariant mass spectrum, and the ALICE Collaboration have determined the $K^-\Lambda$ scattering length from the measurement of the momentum correlation functions in heavy ion collisions. Using the effective range expansion, we classify the nature of the pole of the near-threshold eigenstate in terms of the scattering length, in the presence of the decay channel. It is shown that the quasibound state below the threshold can be described by only the scattering length, while the description of the resonance above the threshold requires the contribution from the effective range. Based on the chiral unitary approach, we construct a theoretical model which generates the pole of $\Xi(1620)$ below the $\bar{K}\Lambda$ threshold with relatively narrow width, as reported by the Belle Collaboration. It is quantitatively demonstrated that the spectrum of the $\Xi(1620)$ quasibound state is distorted by the effect of the nearby $\bar{K}\Lambda$ threshold. We then construct another model which reproduces the $K^-\Lambda$ scattering length by the ALICE Collaboration. In this case, the eigenstate pole does not appear in the physically relevant Riemann sheet, and the spectrum shows a cusp structure at the $\bar{K}\Lambda$ threshold. We finally examine the compatibility of the value of the $\bar{K}\Lambda$ scattering length and the subthreshold pole of $\Xi(1620)$ including the experimental uncertainties.

DOI: 10.1103/PhysRevC.109.015203

I. INTRODUCTION

The Ξ baryon (strangeness $S = -2$, isospin $I = 1/2$) has two charged components, Ξ^0 and Ξ^-, constructed by uss and dss, respectively. While almost thirty excited states are confirmed in the nucleon sector experimentally, only about ten excited Ξ baryons have been established so far [1,2]. Furthermore, the nature of the most of excited Ξ states is not well understood. This is because the study of the excited Ξ states requires double strangeness production, and therefore experimental data have not accumulated very much. In theoretical studies, various model calculations have been performed, but the natures of the excited Ξ states have not been well clarified, due to the lack of experimental data.

Recently, there has been great progress in obtaining detailed data of the low-lying Ξ excited states experimentally. In 2019, the Belle Collaboration observed peaks of $\Xi(1620)$ and $\Xi(1690)$ in the invariant mass distribution of $\pi^+\Xi^-$ in the $\Xi_c \to \Xi^-\pi^+\pi^+$ decay [3]. In 2020, the $\Xi(1690)$ resonance was observed in the ΛK^- invariant mass distribution in the $\Xi_b \to J/\psi \Lambda K^-$ decay by the LHCb Collaboration [4]. In 2021, through the measurement of the two-body momentum correlation function in the Pb-Pb collisions, the ALICE Collaboration reported the scattering length of $K^-\Lambda$, whose threshold energy is close to the mass of $\Xi(1620)$ [5]. It is expected that these detailed data will serve to elucidate the nature of $\Xi(1620)$ and $\Xi(1690)$.

Theoretical studies were performed mainly before these recent experimental developments. For instance, in the constituent quark model [6], the masses of $\Xi(1620)$ and $\Xi(1690)$ are predicted to be much higher than those in Belle and LHCb results. A study by the lattice QCD calculation with $m_\pi \geqslant 225$ MeV obtained reasonable effective masses of the ground state and $\Xi(1535)$, but the signals of other excited states are not conclusive [7]. In contrast to these static frameworks, the chiral unitary approach [8–11] dynamically generates the excited Ξ states as resonances in meson-baryon scattering. In Ref. [12], the mass of $\Xi(1620)$ is obtained at around 1600 MeV, but with a broad width. It is shown in the work of Ref. [13] that $\Xi(1620)$ and $\Xi(1690)$ can be generated simultaneously. Additionally, this work was expanded to an SU(6) model in Ref. [14]. In a model with vector meson-baryon channels, Ref. [15] shows that the narrow width of $\Xi(1690)$ can be explained by small couplings to the decay channels. By focusing on $\Xi(1690)$, Ref. [16] generates a pole near the $\bar{K}\Sigma$ threshold as a hadronic molecule state. It is shown that the model can reproduce the invariant mass distribution of $\bar{K}\Sigma$ and $\bar{K}\Lambda$ in the Λ_c decay [17]. A recent work [18] after the Belle measurement indicates that $\Xi(1620)$ and $\Xi(1690)$ can be reproduced simultaneously by taking into account the next-to-leading order (NLO) chiral interaction, but again with a broad decay width of about 150 MeV for $\Xi(1620)$. It is worth mentioning that a narrow width $\Xi(1620)$ was predicted by the flavor SU(3) symmetry in an analysis of the hypothetical light nucleon resonance N' [19].

---

[*] nishibuchi-takuma@ed.tmu.ac.jp

[†] hyodo@tmu.ac.jp

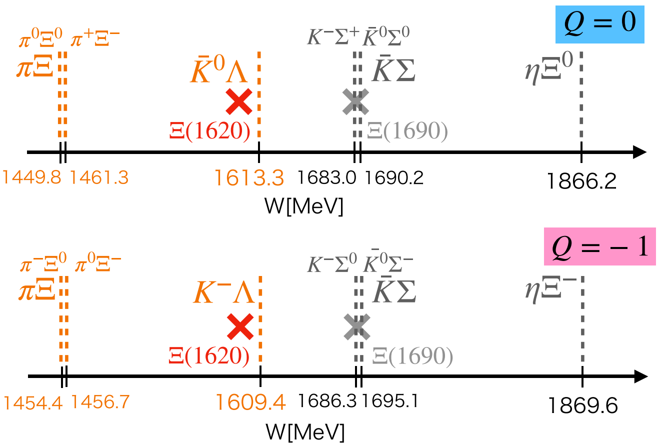

FIG. 1. The threshold energies of the meson-baryon channels with strangeness -2 and the Ξ resonances. The upper (lower) panel shows the neutral channels with $Q = 0$ (charged channels with $Q = -1$).

Given that new data have been obtained by Belle and ALICE, in this paper, we discuss the nature of $\Xi(1620)$ by focusing on the location of the resonance pole in relation to the $K^-\Lambda$ scattering length. For this purpose, we classify the eigenstates[1] near the threshold with respect to the value of the scattering length based on the effective range expansion. We then construct models which reproduce the experimental results by using the chiral unitary approach. First, we construct a model with the $\Xi(1620)$ quasibound state below the threshold having a narrow width as indicated by Belle. Second, we construct a model by reproducing the $K^-\Lambda$ scattering length obtained by ALICE. Note that there are neutral and charged meson-baryon channels for $\Xi^0(1620)$ and $\Xi^-(1620)$, respectively, as shown in Fig. 1. The $\pi^+\Xi^-$ spectrum of Belle corresponds to the neutral channel while the $K^-\Lambda$ scattering length is in the charged channel.

When we investigate the spectrum of $\Xi(1620)$, it is important to pay attention to the effect from the threshold. The peak of $\Xi^0(1620)$ appears near the $\bar{K}^0\Lambda$ threshold at 1613.3 MeV. In general, it is known that the near-threshold spectrum is affected by the existence of the threshold, so we need to consider the threshold effect on the spectrum of the $\Xi(1620)$ resonance. The threshold effects can be examined in the chiral unitary approach, where the threshold dynamics in the coupled-channel meson-baryon scattering is built in.

The outline of this paper is as follows. In Sec. II, we introduce the chiral unitary approach. We then discuss the relation between the complex scattering length and the pole near the threshold through the effective range expansion in Sec. III. In Sec. IV, we first construct a model which generates $\Xi(1620)$ slightly below the $\bar{K}\Lambda$ threshold as indicated by the Belle result (Model 1). Next, using the $K^-\Lambda$ scattering length by ALICE, we construct another model (Model 2) and search for the pole of the scattering amplitude. The classification scheme of Sec. III is applied to the results of Model 1 and Model 2 to investigate the nature of $\Xi(1620)$. Finally, we compare Model 1 with Model 2 by considering the experimental uncertainties in order to explore the model which satisfies both the constrains. In the last section, we summarize this work and present future prospects. The preliminary results of Sec. IV A are reported in a conference proceedings [22].

TABLE I. Group theoretical factor C_{ij} for the neutral channels.

	$K^-\Sigma^+$	$\bar{K}^0\Sigma^0$	$\bar{K}^0\Lambda$	$\pi^+\Xi^-$	$\pi^0\Xi^0$	$\eta\Xi^0$
$K^-\Sigma^+$	1	$-\sqrt{2}$	0	0	$-1/\sqrt{2}$	$-\sqrt{3/2}$
$\bar{K}^0\Sigma^0$	$-\sqrt{2}$	0	0	$-1/\sqrt{2}$	$-1/2$	$\sqrt{3/4}$
$\bar{K}^0\Lambda$	0	0	0	$-\sqrt{3/2}$	$\sqrt{3/4}$	$-3/2$
$\pi^+\Xi^-$	0	$-1/\sqrt{2}$	$-\sqrt{3/2}$	1	$-\sqrt{2}$	0
$\pi^0\Xi^0$	$-1/\sqrt{2}$	$-1/2$	$\sqrt{3/4}$	$-\sqrt{2}$	0	0
$\eta\Xi^0$	$-\sqrt{3/2}$	$\sqrt{3/4}$	$-3/2$	0	0	0

II. FORMULATION OF CHIRAL UNITARY APPROACH

In this section, we formulate the coupled-channel scattering amplitude by the chiral unitary approach [8–11]. In general, the scattering amplitude T_{ij} satisfies the scattering equation

$$T_{ij}(W) = V_{ij}(W) + \sum_k V_{ik}(W)G_k(W)T_{kj}(W), \tag{1}$$

which is written using the loop function $G_k(W)$ and the interaction kernel $V_{ij}(W)$. W is the total energy of the system and the indices i, j, k specify the coupled channel. The meson-baryon scattering channels related to the Ξ resonance with strangeness -2 are $\pi^0\Xi^0$, $\pi^+\Xi^-$, $\bar{K}^0\Lambda$, $K^-\Sigma^+$, $\bar{K}^0\Sigma^0$, and $\eta\Xi^0$ in the neutral channels and $\pi^-\Xi^0$, $\pi^0\Xi^-$, $K^-\Lambda$, $K^-\Sigma^0$, $\bar{K}^0\Sigma^-$, and $\eta\Xi^-$ in the negatively charged channels (Fig. 1). The interaction kernel $V_{ij}(W)$ represents the interaction from j to i channel. In this work, we use the Weinberg-Tomozawa (WT) interaction

$$V_{ij}^{\mathrm{WT}}(W) = -\frac{C_{ij}}{4f_i f_j}(2W - M_i - M_j)\sqrt{\frac{M_i + E_i}{2M_i}}\sqrt{\frac{M_j + E_j}{2M_j}}, \tag{2}$$

which is the leading-order term in chiral perturbation theory, as an s-wave interaction which is dominant at low energy. f_i, M_i, and E_i are the meson decay constant, baryon mass, and energy of the baryon in channel i, respectively. C_{ij} is the group theoretical factor expressing the nature of the interaction. Explicit values of C_{ij} are shown in Tables I and II for neutral and negatively charged channels, respectively.

The loop function $G_k(W)$ is given as follows:

$$G_k(W) = i\int \frac{d^4q}{(2\pi)^4}\frac{2M_k}{(P-q)^2 - M_k^2 + i0^+}\frac{1}{q^2 - m_k^2 + i0^+}, \tag{3}$$

---

[1] In this paper, we use the word "eigenstate" not only for the bound state, but also for unstable states because they are obtained by the same boundary condition for the Schördinger equation [2]. See also Refs. [20,21].

TABLE II. Group theoretical factor C_{ij} for the negatively charged channels.

	$\bar{K}^0\Sigma^-$	$K^-\Sigma^0$	$K^-\Lambda$	$\pi^-\Xi^0$	$\pi^0\Xi^-$	$\eta\Xi^-$
$\bar{K}^0\Sigma^-$	1	$\sqrt{2}$	0	0	$1/\sqrt{2}$	$-\sqrt{3/2}$
$K^-\Sigma^0$	$\sqrt{2}$	0	0	$1/\sqrt{2}$	$-1/2$	$-\sqrt{3/4}$
$K^-\Lambda$	0	0	0	$-\sqrt{3/2}$	$-\sqrt{3/4}$	$-3/2$
$\pi^-\Xi^0$	0	$1/\sqrt{2}$	$-\sqrt{3/2}$	1	$\sqrt{2}$	0
$\pi^0\Xi^-$	$1/\sqrt{2}$	$-1/2$	$-\sqrt{3/4}$	$\sqrt{2}$	0	0
$\eta\Xi^-$	$-\sqrt{3/2}$	$-\sqrt{3/4}$	$-3/2$	0	0	0

where $P^\mu = (W, \mathbf{0})$ is the total four-momentum in the center-of-mass system and m_i is the meson mass in channel i. Because the q integration of the loop function (3) diverges logarithmically, some kind of regularization is required. When we apply the dimensional regularization, the finite part of the loop function is obtained as

$$
\begin{aligned}
G_k&[W; a_k(\mu_{\text{reg}})]\\
&= \frac{2M_k}{16\pi^2}\bigg[a_k(\mu_{\text{reg}}) + \ln\frac{m_k M_k}{\mu_{\text{reg}}^2} + \frac{M_k^2 - m_k^2}{2W^2}\ln\frac{M_k^2}{m_k^2}\\
&\quad + \frac{\lambda^{1/2}}{2W^2}\Big\{\ln\left(W^2 - m_k^2 + M_k^2 + \lambda^{1/2}\right)\\
&\quad + \ln\left(W^2 + m_k^2 - M_k^2 + \lambda^{1/2}\right)\\
&\quad - \ln\left(-W^2 + m_k^2 - M_k^2 + \lambda^{1/2}\right)\\
&\quad - \ln\left(-W^2 - m_k^2 + M_k^2 + \lambda^{1/2}\right)\Big\}\bigg],
\end{aligned}
\tag{4}
$$

$$
\lambda^{1/2} = \sqrt{W^4 + m_k^4 + M_k^4 - 2W^2 m_k^2 - 2m_k^2 M_k^2 - 2M_k^2 W^2},
\tag{5}
$$

where μ_{reg} is the regularization scale and $a_i(\mu_{\text{reg}})$ is the subtraction constant of channel i.

The nonrelativistic scattering amplitude $F_{ij}(W)$ is obtained from $T_{ij}(W)$ in Eq. (1) as

$$
F_{ij}(W) = -\frac{\sqrt{M_i M_j}}{4\pi W} T_{ij}(W).
\tag{6}
$$

The imaginary part of the nonrelativistic scattering amplitude $F_{ij}(W)$ corresponds to the spectrum. The scattering length of channel i is determined by the elastic scattering amplitude at the threshold energy as

$$
a_{0,i} = -F_{ii}(W = m_i + M_i).
\tag{7}
$$

For the interaction kernel V in Eq. (2), effects from the higher order terms in chiral perturbation theory and from higher partial waves can be important when the scattering channels are coupled with large energy difference between thresholds. However, in the meson-baryon scattering with $S = -1$, the experimental results of K^-p scattering can be reproduced with good accuracy by only the s-wave scattering with the WT interaction, although the energy differences between thresholds are as large as that in $S = -2$ [23–25]. In the same way, the previous study including the p-wave interaction concluded that the effects from p wave is very small for meson-baryon scattering with $S = -1$ [26,27]. Therefore, it is expected that the meson-baryon scattering with $S = -2$ can also be written using only the s-wave scattering with the WT interaction, as in the meson-baryon scattering with $S = -1$.

We note that a more precise analysis would require the chiral expansion up to the NLO terms [23–25]. The interaction from the NLO terms which are of higher order than the WT term contains the low energy constants. Experimental results are needed to determine these constants. But, for $S = -2$, there are not enough experimental results to determine the low energy constants in the higher order terms. So, in this work, we performed a minimum calculation only with the WT interaction, which has no free parameters.

III. SCATTERING LENGTH AND POLE POSITION

If a resonance state exists, the scattering amplitude has a pole at the eigenenergy in the complex energy plane. To perform the analytic continuation of the scattering amplitude, it is important to consider the Riemann sheets of the complex energy plane. For a single-channel scattering, the energy corresponding to the upper half of the complex momentum plane is called the [t] sheet (first Riemann sheet), and that corresponding to the lower half is named the [b] sheet (second Riemann sheet) [28]. In the complex energy plane, there is a branch cut on the positive real energy axis with the branch point at the origin. In a general coupled-channel scattering, because the momentum in each channel should be determined for a given energy E, there are two Riemann sheets ([t], [b]) in each coupled channel. Hence, for an n-channel scattering, there are in total 2^n Riemann sheets. We denote the choice of the Riemann sheets as [bbtt$\cdots$] in the ordering of the channels with lower threshold energy. Classification of the eigenstates is important because the effects on the scattering amplitude on the real axis depend on the position and the Riemann sheets of the pole of the eigenstate.

For a near-threshold resonance such as Ξ(1620), it is expected that the scattering length is strongly affected by the presence of the pole of the resonance. In this section, we discuss the relation between the scattering length and the near-threshold pole in a simple two-channel scattering (see also Refs. [28,29]). We first summarize the basic properties of the Riemann sheets of the complex energy plane for the two-channel scattering, and classify the eigenstate represented by the pole of the scattering amplitude in Sec. III A. We then consider the classification of the eigenstate in the corresponding complex momentum plane, in order to express it by the eigenmomentum in Sec. III B. Finally, we relate the eigenmomentum to the scattering length for the classification of the eigenstate in Sec. III C.

A. Eigenstates in complex energy plane

Bearing in mind the $\pi\Xi$-$\bar{K}\Lambda$ system with Ξ(1620) near the $\bar{K}\Lambda$ threshold, we consider the eigenstate near the higher energy threshold. Because the Riemann sheet is specified by the choice of the momentum of each channel, there are four sheets, denoted by [tt], [tb], [bt], and [bb].

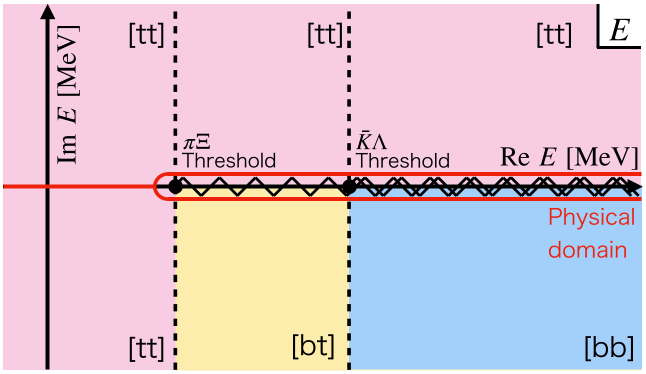

FIG. 2. The physically relevant Riemann sheet of the complex energy plane for the $\pi\Xi$-$\bar{K}\Lambda$ scattering. The solid line represents the physical domain.

Physical scattering occurs for a real and positive momentum (physical domain) in a single-channel scattering. In the complex energy plane, the physical domain exists on the positive real axis between the [t] sheet with positive imaginary part ($E + i\epsilon$ with $\epsilon > 0$) and the [b] sheet with negative imaginary part ($E - i\epsilon$). Below the threshold, the physical domain is analytically continued to the pure imaginary momentum with a positive imaginary part, corresponding to the negative real energy axis in the [t] sheet. In other words, the physical domain is in the [t] sheet for $E + i\epsilon$ for all energies, while for $E - i\epsilon$ it is in the [t] sheet below the threshold and in the [b] sheet above the threshold. Generalizing this for the coupled-channel scattering, the physical domain is connected to the sheet with the choice of [t] for all channels ([tt $\cdots$] sheet) for $E + i\epsilon$ and the sheet with the choice of the [b] ([t]) sheet for the open (closed) channels for $E - i\epsilon$. In the following, we call this the physically relevant Riemann sheet. The physically relevant Riemann sheet for the $\pi\Xi$-$\bar{K}\Lambda$ scattering is illustrated in Fig. 2.

The eigenstate pole can be generated on the real energy axis below the $\pi\Xi$ threshold and the lower half plane above the $\pi\Xi$ threshold. The pole below the $\pi\Xi$ threshold represents the stable bound state (B), and the pole above the $\pi\Xi$ threshold with a finite imaginary part stands for the unstable resonance. In this work, we call the pole between the $\pi\Xi$ and $\bar{K}\Lambda$ thresholds the quasibound state (QB), because it can be interpreted as the bound state in the $\bar{K}\Lambda$ channel, which acquires the decay width through the coupling to the $\pi\Xi$ continuum. Although the quasibound state can be regarded as a resonance in the $\pi\Xi$ scattering, here we use "quasibound state" in order to distinguish it from the pole above the $\bar{K}\Lambda$ threshold, which we call the resonance R. The pole of QB is located on the [bt] sheet, which is different from the [bb] sheet where R exists. In this way, because the Riemann sheet is different, QB below the threshold is not continuously connected to R above the threshold.

In Fig. 3, we show the Riemann sheets of the complex energy plane by setting the $\bar{K}\Lambda$ threshold at the origin. There are four Riemann sheets, [tt], [tb], [bt], and [bb], for the two-channel scattering. Above the $\pi\Xi$ threshold, the physical domain is in the [tt] sheet for $E + i\epsilon$, in the [bt] sheet for $E - i\epsilon$ between the $\pi\Xi$ and $\bar{K}\Lambda$ thresholds, and in the [bb] sheet for $E - i\epsilon$ above the $\bar{K}\Lambda$ threshold.

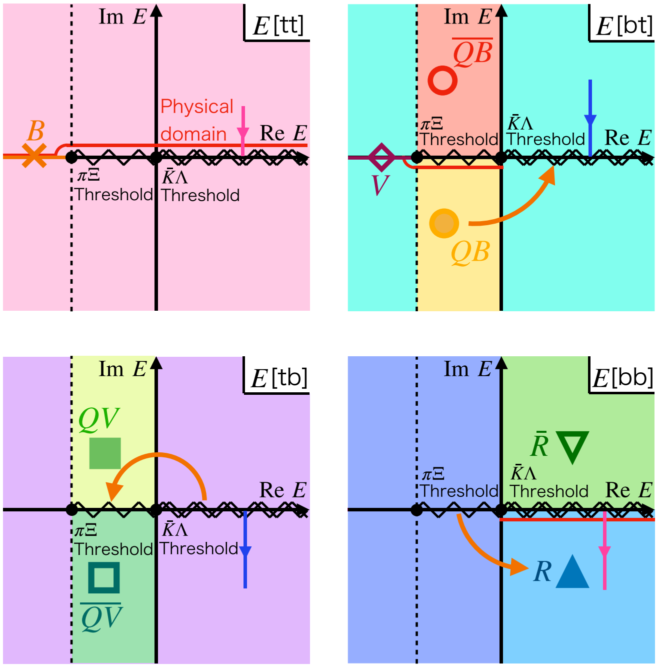

FIG. 3. Riemann sheets of the complex energy plane for the $\pi\Xi$-$\bar{K}\Lambda$ scattering. Poles are classified into B (bound state, cross), V (virtual state, diamond), R (resonance, filled triangle), $\bar{R}$ (antiresonance, open triangle), QB (quasibound state, filled circle), $\overline{QB}$ (quasibound state, open circle), QV (quasivirtual state, filled square), $\overline{QV}$ (antiquasivirtual state, open square). The solid line represents the physical domain.

Next, we classify the eigenstates expressed by the pole of the scattering amplitude. We define the resonance (R) as a pole above the $\bar{K}\Lambda$ threshold in the lower half plane of the [bb] sheet, and the quasibound state (QB) as a pole between the $\pi\Xi$ and $\bar{K}\Lambda$ thresholds in the lower half plane of the [bt] sheet. According to the Schwarz reflection principle, the existence of a pole (either QB or R) in the lower half plane indicates a pole in the upper half plane at the position symmetric with respect to the real axis. The pole accompanied by the resonance is called the anti-resonance ($\bar{R}$), and here we call the one associated with the quasibound state the antiquasibound state ($\overline{QB}$). While R and $\bar{R}$ (QB and $\overline{QB}$) exist at the same distance from the real axis, the pole of R (QB) has stronger effect on the physical scattering because the physical domain is in the lower half plane (see Fig. 3). The stable bound state (B) can be found on the real axis below the $\pi\Xi$ threshold in the [tt] sheet, and the virtual state is in the [bt] sheet.

Let us consider the behavior of the QB pole by gradually adjusting the coupling to the $\pi\Xi$ channel. When the coupling to the $\pi\Xi$ channel is reduced, the width of a quasibound state QB becomes smaller, and the pole approaches the real energy axis. In the zero coupling limit [30], the pole eventually reaches the real axis between the [tt] and [bt] sheets, which is nothing but a bound state in the single $\bar{K}\Lambda$ channel. In the same way, a virtual state in the single $\bar{K}\Lambda$ channel in the zero coupling limit should exist on the real energy axis between

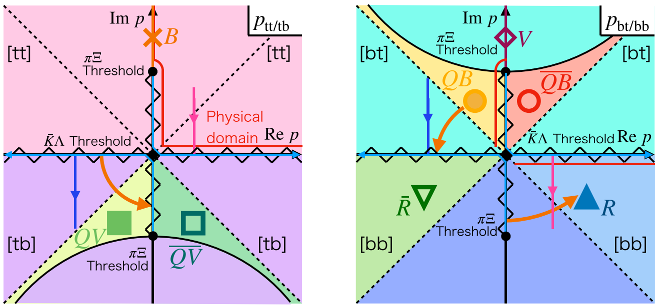

(a)Complex p plane
[tt]-[tb] sheet

(b)Complex p plane
[bt]-[bb] sheet

FIG. 4. Riemann sheets of the complex momentum plane of the $\bar{K}\Lambda$ channel for the $\pi\Xi$-$\bar{K}\Lambda$ scattering. (a) $p_{tt/tb}$ sheet, (b) $p_{bt/bb}$ sheet. Poles are classified into B (bound state, cross), V (virtual state, diamond), R (resonance, filled triangle), $\bar{R}$ (antiresonance, open triangle), QB (quasibound state, filled circle), $\overline{QB}$ (quasibound state, open circle), QV (quasivirtual state, filled square), $\overline{QV}$ (antiquasivirtual state, open square). The solid line represents the physical domain.

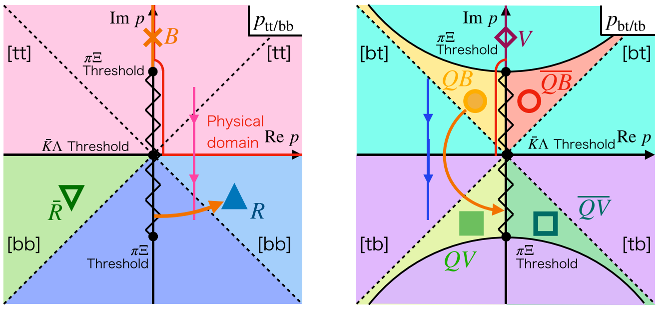

(a)Complex p plane
[tt]-[bb] sheet

(b)Complex p plane
[bt]-[tb] sheet

FIG. 5. Riemann sheets of the complex momentum plane of the $\bar{K}\Lambda$ channel for the $\pi\Xi$-$\bar{K}\Lambda$ scattering. (a) $p_{tt/bb}$ sheet, (b) $p_{bt/bb}$ sheet. Poles are classified into B (bound state, cross), V (virtual state, diamond), R (resonance, filled triangle), $\bar{R}$ (antiresonance, open triangle), QB (quasibound state, filled circle), $\overline{QB}$ (quasibound state, open circle), QV (quasivirtual state, filled square), $\overline{QV}$ (antiquasivirtual state, open square). The solid line represents the physical domain.

the [tb] and [bb] sheets. When the coupling to the $\pi\Xi$ channel is switched on, it is expected that the virtual state pole moves into the complex energy plane of the [tb] sheet.[2] We call this pole the "quasivirtual state" (QV), which is a would-be virtual state in the absence of the channel coupling.

Some remarks on the quasivirtual state QV are in order. First, because the pole of QV is not on the physically relevant Riemann sheet shown in Fig. 2, we do not expect the peak structure in the corresponding spectrum on the real axis. Nevertheless, the existence of a quasivirtual pole near the threshold implies a strong cusp effect at the $\bar{K}\Lambda$ threshold [29]. Second, when we consider the transition from the quasibound state QB to the resonance R, the expected pole trajectory goes through the quasivirtual state QV as indicated by the arrows in Fig. 3 (see Ref. [28]). This is analogous to the transition from the bound state to the resonance through the virtual state in the single-channel scattering [31–33]. Third, the imaginary part of the QV pole is positive, in contrast to QB and R which have a negative imaginary part. From the discussion of the pole trajectory, it is clear that the pole with a positive imaginary part (QV) is closer to the physical domain than that with a negative imaginary part ($\overline{QV}$).

B. Eigenstates in complex momentum plane

Next, we consider the same classification of the eigenstate pole in the complex momentum plane. The complex momentum plane of the $\bar{K}\Lambda$ channel has two Riemann sheets to specify the sign of the $\pi\Xi$ momentum. In Fig. 4 we show two complex momentum planes of the $\bar{K}\Lambda$ channel. In panel (a), the Riemann sheet of the $\pi\Xi$ channel is fixed to the [t] sheet, and (b) to the [b] sheet. The upper half plane of Fig. 4 (a) corresponds to the [tt] sheet of the complex energy plane, and the lower half plane to the [tb] sheet. We therefore call (a) the complex $p_{\rm tt/tb}$ plane and (b) the $p_{\rm bt/bb}$ plane.

By measuring the energy E from the $\bar{K}\Lambda$ threshold, the $\pi\Xi$ threshold energy is negative, $E=-\Delta$ with $\Delta>0$. Since the relation between the $\bar{K}\Lambda$ momentum p and the energy E is $p=\pm\sqrt{2\mu E}$, the pure imaginary momenta $p=\pm i\sqrt{2\mu\Delta}$ correspond to the $\pi\Xi$ threshold, as seen in Fig. 4. In the complex energy plane, the branch cut runs from the threshold on the positive real energy axis. In the complex momentum plane in Fig. 4, the branch cuts run also from the threshold momenta to $\pm\infty$ on the real axis. The cut on the real axis in Fig. 4(a) indicates that the [tt] sheet is not directly connected to the [tb] sheet (see also Fig. 3). In the same way, the [bt] sheet is separated from the [bb] sheet by the branch cut in panel (b). The cut on the real axis in Fig. 4 can be eliminated by exchanging the lower half plane, as shown in Fig. 5. The complex $p_{\rm tt/bb}$ plane consists of the [tt] sheet in the upper half plane and the [bb] sheet in the lower half plane, and $p_{\rm bt/tb}$ consists of the [bt] sheet in the upper half plane and the [tb] sheet in the lower half plane. In this case, the upper and lower half planes are smoothly connected without the cut.

We then classify the eigenstates in the complex momentum plane. The poles of the quasibound state QB and $\overline{QB}$ appear in the upper half plane of the $p_{\rm bt/tb}$ sheet in Fig. 5. By denoting the phases of the complex momentum p and the energy E with respect to the $\bar{K}\Lambda$ threshold as

$$p=|p|e^{i\theta_p},\quad E=|E|e^{i\theta_E}, \tag{8}$$

the relation $E=p^2/(2\mu)$ leads to

$$2\theta_p=\theta_E, \tag{9}$$

where μ is the reduced mass of the $\bar{K}\Lambda$ channel. From the [bt] sheet of the complex energy plane in Fig. 3, the phase of the energy θ_E of QB is restricted as $\pi\leqslant\theta_E\leqslant 3\pi/2$. Equation (9)

---

[2] In principle, the virtual pole can move into the [bb] sheet, but, as we shall show below, the pole on the [bb] sheet cannot be reproduced only by the scattering length. We therefore expect that the near-threshold quasivirtual pole should move into the [tb] sheet.

then gives the corresponding phase of the momentum as

$$QB: \quad \frac{\pi}{2} \leqslant \theta_p \leqslant \frac{3}{4}\pi \quad \text{[bt]}. \tag{10}$$

In addition, because the QB pole should appear above the $\pi\Xi$ threshold energy $E = -\Delta$, the condition $-\Delta \leqslant \mathrm{Re}\, E$ holds. Denoting the complex momentum as $p = \gamma + i\kappa$ with $\gamma, \kappa \in \mathbb{R}$, this condition can be expressed as

$$-\sqrt{\gamma^2 + 2\mu\Delta} \leqslant \kappa \leqslant \sqrt{\gamma^2 + 2\mu\Delta}. \tag{11}$$

Namely, the QB pole can be found in the $p_{\text{bt/bb}}$ plane below the hyperbola $\kappa = \sqrt{\gamma^2 + 2\mu\Delta}$ with (10), as shown in Fig. 5(b). The allowed region for the pole of $\overline{QB}$ should be symmetric with respect to the imaginary axis, as shown in Fig. 5(b).

For the resonance R, the pole should appear above the $\bar{K}\Lambda$ threshold and its phase of the complex energy satisfies

$$\tfrac{7}{2}\pi \leqslant \theta_E \leqslant 4\pi. \tag{12}$$

The corresponding phase of the momentum is restricted as

$$R: \quad \tfrac{7}{4}\pi \leqslant \theta_p \leqslant 2\pi \quad \text{[bb]}. \tag{13}$$

The pole region for the quasivirtual state QV is obtained in the same manner as the quasibound state QB. The allowed phase of the eigenenergy is

$$\tfrac{5}{2}\pi \leqslant \theta_E \leqslant 3\pi, \tag{14}$$

which leads to

$$QV: \quad \tfrac{5}{4}\pi \leqslant \theta_p \leqslant \tfrac{3}{2}\pi \,\text{[tb]}, \tag{15}$$

and the condition $-\Delta < \mathrm{Re}\, E$ is given by

$$-\sqrt{\gamma^2 + 2\mu\Delta} \leqslant \kappa. \tag{16}$$

C. Relation with scattering length

Now we are in a position to relate the eigenmomentum with the scattering length. The scattering length of the higher energy ($\bar{K}\Lambda$) channel a_0 is determined by the elastic scattering amplitude at the threshold as in Eq. (7). In contrast to the single-channel scattering where the scattering length a_0 is real, the scattering length has an imaginary part when the coupling to the lower energy decay channel is switched on. Note that the sign of the imaginary part of a_0 is shown to be negative due to the optical theorem.

When the magnitude of the scattering length $|a_0|$ is sufficiently large, the near-threshold scattering amplitude can be approximated as $f(p) = (-1/a_0 - ip)^{-1}$, and the pole of the scattering amplitude is given by

$$p = \frac{i}{a_0}. \tag{17}$$

To relate this with the classification of the eigenstate, we define the phase of the scattering length θ_{a_0} as

$$a_0 = |a_0| e^{i\theta_{a_0}}. \tag{18}$$

From Eq. (17), the relation between θ_{a_0} and θ_p is given by

$$\theta_{a_0} = \frac{\pi}{2} - \theta_p. \tag{19}$$

Thus, the conditions in Eqs. (10), (13), and (15) are translated into those for θ_{a_0} as

$$\begin{aligned} QB: &\quad \frac{7\pi}{4} \leqslant \theta_{a_0} \leqslant 2\pi, \\ R: &\quad \frac{\pi}{2} \leqslant \theta_{a_0} \leqslant \frac{3\pi}{4}, \\ QV: &\quad \pi \leqslant \theta_{a_0} \leqslant \frac{5\pi}{4}. \end{aligned} \tag{20}$$

Namely, when the scattering amplitude has the quasibound state QB, the real part of the scattering length is positive and the imaginary part is negative with a smaller magnitude than the real part. For the resonance R, the imaginary part is positive and the real part is negative with a smaller magnitude than the imaginary part. For the quasivirtual state QV, both the real and imaginary parts are negative with the real part having the larger magnitude than the imaginary part. These can be summarized as

$$\begin{aligned} QB: &\quad \mathrm{Re}\, a_0 > 0, \quad \mathrm{Im}\, a_0 < 0, \quad |\mathrm{Im}\, a_0| < \mathrm{Re}\, a_0, \\ R: &\quad \mathrm{Re}\, a_0 < 0, \quad \mathrm{Im}\, a_0 > 0, \quad |\mathrm{Re}\, a_0| < \mathrm{Im}\, a_0, \\ QV: &\quad \mathrm{Re}\, a_0 < 0, \quad \mathrm{Im}\, a_0 < 0, \quad |\mathrm{Im}\, a_0| < |\mathrm{Re}\, a_0|. \end{aligned} \tag{21}$$

The result for R, however, shows the positive imaginary part, which contradicts with the optical theorem. This indicates that the resonance R above the $\bar{K}\Lambda$ threshold cannot be described by the approximation $f(p) = (-1/a_0 - ip)^{-1}$, and the contribution from the effective range is necessary.

In general, the phase of the scattering length θ_{a_0} is related to the Riemann sheet as

$$\begin{aligned} \frac{\pi}{2} \leqslant \theta_{a_0} \leqslant \pi: &\quad \text{[bb]}, \\ \pi \leqslant \theta_{a_0} \leqslant \frac{3}{2}\pi: &\quad \text{[tb]}, \\ \frac{3\pi}{2} \leqslant \theta_{a_0} \leqslant 2\pi: &\quad \text{[bt]}, \end{aligned} \tag{22}$$

which can be expressed by the real and imaginary parts of the scattering length as

$$\begin{aligned} \mathrm{Re}\, a_0 < 0, \quad \mathrm{Im}\, a_0 > 0: &\quad \text{[bb]}, \\ \mathrm{Re}\, a_0 < 0, \quad \mathrm{Im}\, a_0 < 0: &\quad \text{[tb]}, \\ \mathrm{Re}\, a_0 > 0, \quad \mathrm{Im}\, a_0 < 0: &\quad \text{[bt]}. \end{aligned} \tag{23}$$

As mentioned above, the scattering length for the pole in the [bb] sheet does not satisfy the optical theorem, and therefore this pole cannot be represented by the scattering amplitude approximated only with the scattering length.

When the effective range r_e is included, the inverse scattering amplitude can be expanded by neglecting the $\mathcal{O}(p^4)$ terms as

$$f(p) = \frac{1}{-\frac{1}{a_0} + \frac{r_e}{2}p^2 - ip}, \tag{24}$$

where the pole of the scattering amplitude is obtained as

$$p = \frac{i \pm \sqrt{-1 + \frac{2r_e}{a_0}}}{r_e}. \tag{25}$$

TABLE III. Subtraction constants of Model 1, Model 2, and Set 1 in Ref. [12].

	$a_{\pi\Xi}$	$a_{\bar{K}\Lambda}$	$a_{\bar{K}\Sigma}$	$a_{\eta\Xi}$
Ref. [12] Set 1	−2.00	−2.00	−2.00	−2.00
Model 1	−4.26	−0.12	−2.00	−2.00
Model 2	−2.90	0.36	−2.00	−2.00

In this case, the resonance pole R in the [bb] sheet can be realized thanks to the contribution from the effective range. In other words, the description of R requires the contribution of the effective range r_e in addition to the scattering length a_0. In fact, it is known for the single-channel scattering that a negative effective range with a large magnitude is needed to obtain a narrow resonance above the threshold [31].

IV. NUMERICAL RESULTS

A. Model 1: Narrow width Ξ(1620)

In this section, based on the previous work of the chiral unitary approach [12], we construct a model which generates the Ξ(1620) resonance in accordance with the Belle result. The reported values of the mass M_R and decay width Γ_R of Ξ(1620) are as follows [3]:

$$M_R = 1610.4 \pm 6.0(\text{stat.})^{+6.1}_{-4.2}(\text{syst.})\text{ MeV},$$

$$\Gamma_R = 59.9 \pm 4.8(\text{stat.})^{+2.8}_{-7.1}(\text{syst.})\text{ MeV}. \tag{26}$$

The pole position z_{ex} corresponding to the central values of Eq. (26) is determined as

$$z_{\text{ex}} = 1610 - 30i\text{ MeV}, \tag{27}$$

which is lower than the $\bar{K}^0\Lambda$ threshold at 1613.3 MeV. In this case, therefore, Ξ(1620) is classified as the quasibound state QB. We aim at constructing the model with a pole at z_{ex}, starting from Set 1 in Ref. [12], which has a pole at $1607 - 140i$ MeV.

Numerical calculations are performed in the physical basis for the neutral channels with $Q = 0$ because the Belle result has been obtained from the $\pi^+\Xi^-$ spectrum [3]. In this case, there are six meson-baryon channels, as shown in Fig. 1. The masses of hadrons are taken from Particle Data Group (PDG) [1], including the isospin symmetry breaking effect. We set the meson decay constants as $f_\pi = f_K = f_\eta = 104.439$ MeV according to Ref. [12].

The subtraction constant a_i at the regularization scale $\mu_{\text{reg}} = 630$ MeV can be used to adjust the model to reproduce the pole position (27). Here we do not consider the isospin symmetry breaking in a_i, and treat four constants shown in Table III. By examining the dependence of the Ξ(1620) pole position on the subtraction constants, we find that the pole depends strongly on the subtraction constants in the $\pi\Xi$ and $\bar{K}\Lambda$ channels, while it is insensitive to those in the $\bar{K}\Sigma$ and $\eta\Xi$ channels. In fact, varying the subtraction constant of channel i in the region $-1.5 \leqslant a_i \leqslant -2.5$ while keeping other constants as -2, we find that the pole position moves about several tens of MeV by changing $a_{\pi\Xi}$ or $a_{\bar{K}\Lambda}$. On the other hand, the pole position moves at most several MeV with the change of $a_{\bar{K}\Sigma}$ or $a_{\eta\Xi}$. In Table IV, we show the quantitative deviation of the pole position $\delta z = |z - z_{\text{ini}}|$ from the initial point $z_{\text{ini}} = 1607 - 140i$ MeV, obtained with all $a_i = -2$. This can be understood from the fact that the energy of the Ξ(1620) pole is close to the $\pi\Xi$ and $\bar{K}\Lambda$ thresholds, as shown in Fig. 1. Hence, in this work, we fix $a_{\bar{K}\Sigma} = a_{\eta\Xi} = -2$ as in Ref. [12], and adjust $a_{\pi\Xi}$ and $a_{\bar{K}\Lambda}$ to reproduce the pole position in Eq. (27).

TABLE IV. Deviation of pole position δz with variation of the subtraction constant a_i.

	$a_{\pi\Xi}$	$a_{\bar{K}\lambda}$	$a_{\bar{K}\Sigma}$	$a_{\eta\Xi}$
δz (MeV)	46–57	28–47	5–6	2–5

Denoting the pole position in the theoretical model as z_{th}, we define the distance of z_{th} from Eq. (27) in the complex energy plane as

$$\Delta z = |z_{\text{th}} - z_{\text{ex}}|.$$

Because z_{th} depends on the subtraction constants, we search for $(a_{\pi\Xi}, a_{\bar{K}\Lambda})$ which minimize Δz. In Fig. 6, we show the density plot of Δz in the $a_{\pi\Xi}$-$a_{\bar{K}\Lambda}$ plane. Note that the pole can move to the region above the $\bar{K}^0\Lambda$ threshold in the [bbtttt] sheet. If the pole locates above the threshold energy, the nature of the solution is qualitatively different. Thus, we formally set Δz to 100 MeV to reject such qualitatively different solutions. Because z_{ex} is very close to the $\bar{K}^0\Lambda$ threshold, near the best-fit region, Δz abruptly changes to the large value. Δz can be minimized with $a_{\pi\Xi} = -4.26$ and $a_{\bar{K}\Lambda} = -0.12$, giving the pole position at

$$z_{\text{th}} = 1610 - 30i\text{ MeV}, \tag{28}$$

which reproduces Eq. (27) with 1 MeV precision. In the following, this parameter set is called Model 1. The subtraction constants are summarized in Table III together with those of Set 1 in Ref. [12].

To examine the peak structure of the spectrum on the real axis, we plot the scattering amplitude in Fig. 7 in comparison with Set 1 in Ref. [12]. The real and imaginary parts of the elastic $\pi^+\Xi^-$ scattering amplitude $F(W)$ defined in Eq. (6)

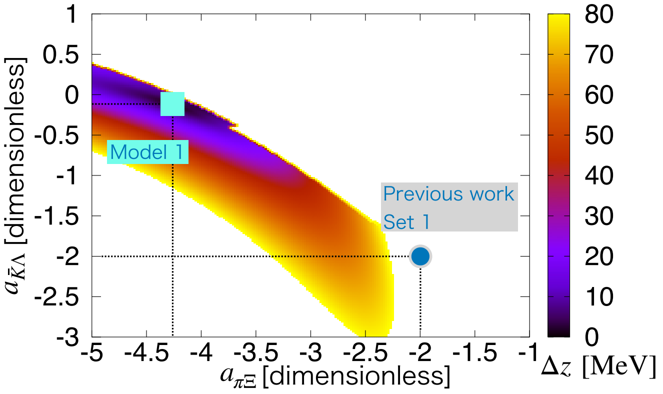

FIG. 6. Density plot of Δz in the $a_{\pi\Xi}$-$a_{\bar{K}\Lambda}$ plane. The square (circle) denotes the parameters of Model 1 (Set 1 in Ref. [12]).

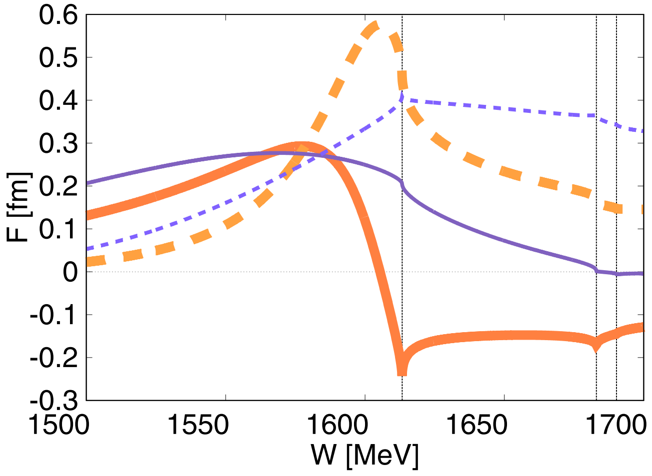

FIG. 7. Comparison of the $\pi^+\Xi^-$ elastic scattering amplitude of Model 1 (thick lines) with that of Set 1 in Ref. [12] (thin lines). Solid (dashed) lines stand for the real (imaginary) parts. Vertical dotted lines represent the thresholds of $\bar{K}^0\Lambda$, $K^-\Sigma^+$, $\bar{K}^0\Sigma^0$ from left to right.

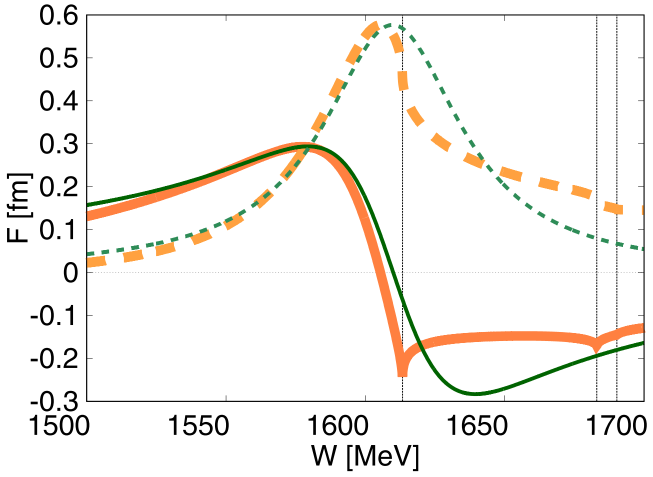

FIG. 8. Comparison of the $\pi^+\Xi^-$ elastic scattering amplitude of Model 1 (thick lines) with the Breit-Wigner amplitude having the pole at the same position (thin lines). Solid (dashed) lines stand for the real (imaginary) parts. Vertical dotted lines represent the thresholds of $\bar{K}^0\Lambda$, $K^-\Sigma^+$, $\bar{K}^0\Sigma^0$ from left to right.

are shown as functions of the total energy W. The imaginary part of the amplitude of Ref. [12] (thin dashed line) does not show a prominent peak structure at the real part of the pole position (1607 MeV). This is because the large magnitude of the imaginary part ($-140i$ MeV) suppresses the effect of the pole on the real energy axis. In contrast, the result of Model 1 (thick lines) shows a typical resonance behavior of the scattering amplitude; the peak of the imaginary part and the zero of the real part at around $W = \text{Re}\, z_{\text{th}} = 1610$ MeV. In this way, we construct the model of chiral unitary approach which generates the $\Xi(1620)$ quasibound state with a relatively narrow width, as indicated by the Belle result.

It should, however, be noted that the position of the $\Xi(1620)$ pole is very close to the $\bar{K}^0\Lambda$ threshold at 1613.3 MeV. In general, the peak near the threshold is known to be distorted by the effect of the threshold. To examine the threshold effect in Model 1, we plot the scattering amplitude of Model 1 together with the Breit-Wigner amplitude having a pole at the same position in Fig. 8. From the comparison of the imaginary parts in Fig. 8, we find that the peak of Model 1 is distorted by the presence of the $\bar{K}^0\Lambda$ threshold. In fact, the peak of Model 1 is at 1606 MeV, which is shifted about 4 MeV downward from the real part of the pole position (1610 MeV). In this way, we quantitatively show the $\bar{K}\Lambda$ threshold effect on the $\Xi(1620)$. This result indicates the importance of the threshold effect for the discussion on the mass and width of the near-threshold quasibound state.

So far we have discussed the model of $\Xi(1620)$ in the neutral meson-baryon channels where the pole (1610 MeV) is slightly below the $\bar{K}^0\Lambda$ threshold (1613.3 MeV). It is worth studying the $\Xi(1620)$ state in the negative charge channel where the threshold of the $K^-\Lambda$ is at 1609.4 MeV, which is lower than the pole of the neutral channel. We calculate the $Q = -1$ scattering amplitude with the C_{ij} coefficients in Table II and the corresponding hadron masses, using the same subtraction constants as Model 1. The pole of the scattering amplitude is obtained at

$$z_{\text{th}} = 1607 - 29i\ \text{MeV}(Q = -1), \tag{29}$$

which is lower than the $K^-\Lambda$ threshold. Namely, the negatively charged $\Xi(1620)$ is obtained also as a quasibound state, as in the $Q = 0$ channel.

B. Model 2: $K^-\Lambda$ scattering length

The ALICE experiment determines the $K^-\Lambda$ scattering length from the measurement of the correlation functions in the high-energy heavy ion collisions. The scattering length is obtained as [5]

$$\begin{aligned}\text{Re}\, f_0 &= 0.27 \pm 0.12(\text{stat.}) \pm 0.07(\text{syst.})\ \text{fm},\\ \text{Im}\, f_0 &= 0.40 \pm 0.11(\text{stat.}) \pm 0.07(\text{syst.})\ \text{fm},\end{aligned} \tag{30}$$

where f_0 is related to the scattering length in Eq. (7) as $a_0 = -f_0$. In general, because the scattering length determines the real and imaginary parts of the scattering amplitude directly, it gives a stronger constraint on theoretical models than the fit to the spectrum. In the numerical calculation, we again adopt the physical basis with $Q = -1$, which contains the $K^-\Lambda$ channel as shown in Fig. 1. As before, isospin symmetric subtraction constants are used.

First, we compare the scattering lengths of Set 1 in Ref. [12] and Model 1 with the result of the ALICE data. The central value of the ALICE measurement in the convention of a_0 is given by

$$a_{0,\text{ex}} = -0.27 - 0.40i\ \text{fm}. \tag{31}$$

The result of the $K^-\Lambda$ scattering length of Set 1 is $a_0 = 0.07 - 0.21i$ fm and that of Model 1 is $a_0 = 0.80 - 0.92i$ fm, in disagreement with the ALICE result in Eq. (31).

Here we construct a model which reproduces Eq. (31). As in the previous section, we optimize the subtraction constants in the $\pi\Xi$ and $\bar{K}\Lambda$ channels with $a_{\bar{K}\Sigma} = a_{\eta\Xi} = -2$ to repro-

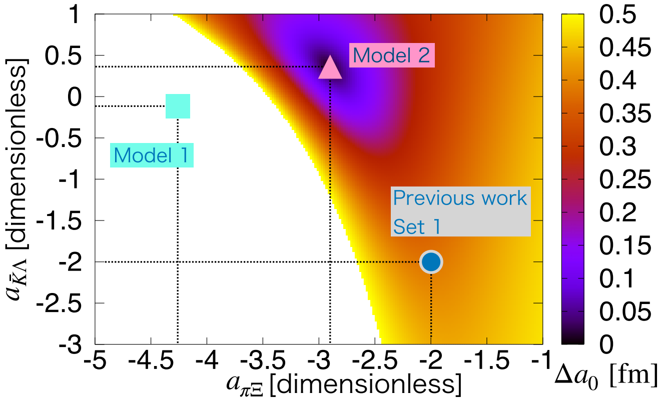

FIG. 9. Density plot of Δa_0 in the $a_{\pi\Xi}$-$a_{\bar{K}\Lambda}$ plane. The triangle, square, and circle denote the parameters of Model 2, Model 1, and Set 1 in Ref. [12].

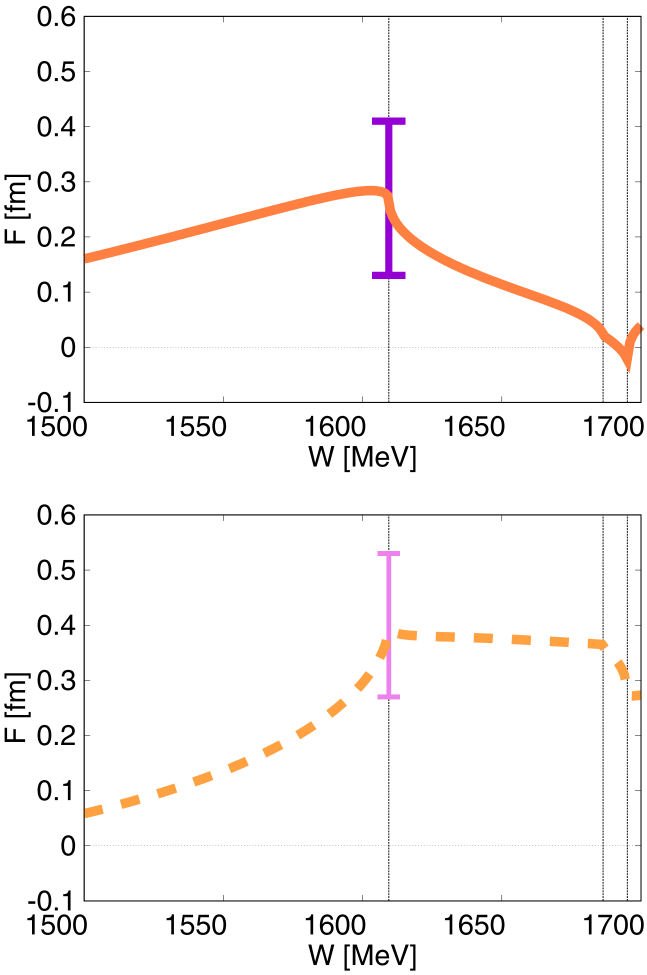

FIG. 10. $K^-\Lambda$ elastic scattering amplitude. Solid (dashed) lines stand for the real (imaginary) parts. The real and imaginary parts of the $K^-\Lambda$ scattering length by the ALICE Collaboration [5] are shown by the error bars using (38). Vertical dotted lines represent the thresholds of $\bar{K}^0\Lambda$, $K^-\Sigma^+$, $\bar{K}^0\Sigma^0$ from left to right.

duce the scattering length. Denoting the scattering length in the theoretical model as $a_{0,\mathrm{th}}$, we define its deviation from the experimental data of $a_{0,\mathrm{ex}}$ in Eq. (31) as

$$\Delta a_0 = |a_{0,\mathrm{th}} - a_{0,\mathrm{ex}}|. \tag{32}$$

To search for the set of $a_{\pi\Xi}$ and $a_{\bar{K}\Lambda}$ which minimize Δa_0, we show the density plot of Δa_0 in the $a_{\pi\Xi}$-$a_{\bar{K}\Lambda}$ plane in Fig. 9. We find the optimized subtraction constants at $a_{\pi\Xi} = -2.90$ and $a_{\bar{K}\Lambda} = 0.36$, which gives the $K^-\Lambda$ scattering length as

$$a_{0,\mathrm{th}} = -0.27 - 0.40i \text{ fm}, \tag{33}$$

which reproduces $a_{0,\mathrm{ex}}$ in the accuracy of 0.01 fm. This is called Model 2 in the following. In Table III, we show the subtraction constants of Model 1 and Model 2 in comparison with those of Set 1 in Ref. [12].

Figure 9 and Table III indicate that the subtraction constants of Model 2 are different from those of Model 1 and Set 1 in Ref. [12]. To study the behavior of the spectrum, we plot the real and imaginary parts of the $K^-\Lambda$ elastic scattering amplitude in Fig. 10 together with the scattering length measured by the ALICE Collaboration indicated by the error bar. The $K^-\Lambda$ elastic scattering amplitude of Model 2 goes across the error bars at the threshold, but shows a different behavior from that of Model 1 in Fig. 7. The spectrum obtained in the experiment corresponds to the imaginary part in Fig. 10, which shows a cusp at the threshold without a clear peak structure. This may be caused by the pole with a large decay width as in Set 1 in Ref. [12], but may also be accompanied by the quasivirtual pole as discussed in Sec. III.

We therefore search for the pole of the scattering amplitude in the complex energy plane. First, we investigate the physically relevant sheet: the [bbtttt] sheet below the $K^-\Lambda$ threshold and the [bbbttt] sheet above the threshold. In this sheet, no pole is found in the energy region $1500 \leqslant \mathrm{Re}\, W \leqslant 1700$ MeV and $0 \leqslant |\mathrm{Im}\, W| \leqslant 100$ MeV. Next, we look for the pole in the [bbtttt], [bbbttt], and [ttbttt] sheets in the energy region $1400 \leqslant \mathrm{Re}\, W \leqslant 1700$ MeV and $0 \leqslant |\mathrm{Im}\, W| \leqslant 300$ MeV. A pole is found in the [ttbttt] at[3]

$$z = 1725 + 76i \text{ MeV}, \tag{34}$$

which corresponds to the quasivirtual (QV) state discussed in Sec. III.

We also calculate the scattering length of the neutral $\bar{K}^0\Lambda$ channel, using the same subtraction constants with the Model 2. The result is

$$a_0 = -0.27 - 0.40i \text{ fm}, \quad (\bar{K}^0\Lambda). \tag{35}$$

To study the isospin breaking effects, we summarize the $\bar{K}\Lambda$ scattering lengths and the pole positions of Ξ(1620) in different charge sectors in Table V. Isospin symmetry breaking effect is of the order of 10^{-2} fm in the scattering length and

---

[3] In the [ttbttt] sheet, there is also a pole at $1725 - 76i$ MeV. As discussed in Sec. III, the pole with a negative imaginary part corresponds to the $\overline{QV}$ state. In Eq. (34), we present the pole in the upper half plane which is connected to R and QB continuously.

TABLE V. Isospin symmetry breaking effects in the $\bar{K}\Lambda$ scattering length and the pole position of $\Xi(1620)$.

	Model 1	Model 2
$a_{\bar{K}^0\Lambda}$ (fm)	$0.80 - 0.89i$	$-0.27 - 0.40i$
$a_{K^-\Lambda}$ (fm)	$0.80 - 0.92i$	$-0.27 - 0.40i$
$\Xi^0(1620)$ (MeV)	$1610 - 30i$	$1726 + 80i$
$\Xi^-(1620)$ (MeV)	$1607 - 29i$	$1725 + 76i$

a few MeV in the pole position. In Model 1, the $\Xi(1620)$ pole is near the $\bar{K}\Lambda$ threshold, and hence the magnitude of the scattering length is enhanced. As a consequence, the isospin symmetry breaking effect in the scattering length is also enhanced. On the other hand, in Model 2, there is no significant isospin breaking effect in the $\bar{K}\Lambda$ scattering length, because the $\Xi(1620)$ pole is not close to the threshold.

C. $K^-\Lambda$ scattering length and $\Xi(1620)$ pole

As shown in Sec. III, the pole near the threshold is closely related to the scattering length. In this section, we discuss the nature of the $\Xi(1620)$ state in Model 1 and Model 2 in relation with the $K^-\Lambda$ scattering length. In Table VI, we summarize the scattering length a_0 and its magnitude $|a_0|$ of Model 1 and Model 2. It is seen that Model 1 has larger magnitude $|a_0|$, reflecting the closer $\Xi(1620)$ pole to the threshold. From the discussion in Sec. III C, when the magnitude of $|a_0|$ is sufficiently large, the energy of the pole z can be estimated as

$$z = \frac{-1}{2\mu_{K^-\Lambda}a_0^2} + M_\Lambda + m_{K^-}, \tag{36}$$

where $\mu_{K^-\Lambda} = 1/[1/m_{K^-} + 1/M_\Lambda]$ is the reduced mass of the $K^-\Lambda$ system.

The pole positions estimated by Eq. (36) from the scattering length are also shown in Table VI together with the exact pole positions in Eqs. (29) and (34). The estimated result of Model 1 ($1615 - 38i$ MeV) is obtained close to the exact pole position at $1607 - 29i$ MeV. This reflects the large magnitude of the scattering length. The deviation of about 10 MeV is caused by the contribution from the higher order terms in the effective range expansion. On the other hand, Eq. (36) gives a pole on the [ttbttt] sheet, because both the real and imaginary parts of the scattering length of Model 2 are negative. In this case, the discussion in Sec. III indicates that the pole is not on the physically relevant Riemann sheet. This is in agreement with the exact pole in the [ttbttt] sheet found in Sec. IV B. At the same time, the position of the estimated pole substantially deviates from the exact one. In order for the estimation (36) to work, the magnitude of the scattering length should be sufficiently large. In Model 2, the magnitude is as small as 0.48 fm, which causes the deviation of about 150 MeV.

In the following, we discuss the ALICE scattering length in relation with the quasibound (*QB*) state near the $K^-\Lambda$ threshold, based on Eq. (36). First, we consider the narrow width *QB* state near the $K^-\Lambda$ threshold with small $|E| = |z - M_\Lambda - m_{K^-}|$. Equation (36) gives an accurate result when $|E|$ is small, i.e., when the pole locates close to the $K^-\Lambda$ threshold. In other words, the scattering length can be estimated from the position of the near-threshold pole. For example, if a pole is located at about 1 MeV from the threshold in the complex energy plane, the absolute value of the scattering length $|a_0|$ will be about 6 fm, and if a pole is located at about 10 MeV away, $|a_0|$ will be about 2 fm. Equation (21) shows that the scattering length corresponding to the *QB* state has a positive real part.

On the other hand, the ALICE gives the $K^-\Lambda$ scattering length as $-0.27 - 0.40i$ fm, with negative real part and small absolute value $|a_0| \approx 0.48$ fm. In principle, it is possible to have a *QB* pole with a small scattering length with negative real part due to the effects from the higher order terms, but it is expected that such cases are not realized, unless the higher order terms of the effective range expansion are fine tuned. Based on the above discussion, we expect that there is unlikely to be a pole near the $K^-\Lambda$ threshold with the ALICE scattering length ($|a_0| \approx 0.48$), when the contribution from the higher order terms of the effective range expansion is small.

D. Comparison of Model 1 with Model 2

We have constructed Model 1 which has the $\Xi(1620)$ quasibound state with a narrow width as indicated by the Belle data in Sec. IV A and Model 2 which reproduces the $K^-\Lambda$ scattering length of the ALICE measurement in Sec. IV B. While both Model 1 and Model 2 are based on experimental data, the fitted values of the subtraction constants show a sizable difference. Here we try to construct a model which satisfies both the constraints by taking into account the experimental uncertainties.

First, we determine the constraints on the pole position by taking the quadrature of the statistical and systematic uncertainties of the Belle result (26):

$$\begin{aligned} 1603.1\ \text{MeV} \leqslant \operatorname{Re} z_{\text{th}} \leqslant 1616.5\ \text{MeV}, \\ \text{and} \quad 25.7\ \text{MeV} \leqslant \operatorname{Im} z_{\text{th}} \leqslant 32.8\ \text{MeV}. \end{aligned} \tag{37}$$

In the same way, the $K^-\Lambda$ scattering length from Eq. (30) is

$$\begin{aligned} -0.41\ \text{fm} \leqslant \operatorname{Re} a_{0,\text{th}} \leqslant -0.13\ \text{fm}, \\ \text{and} \quad -0.53\ \text{fm} \leqslant \operatorname{Im} a_{0,\text{th}} \leqslant -0.27\ \text{fm}. \end{aligned} \tag{38}$$

In Fig. 11, we show the region of the subtraction constants which gives the $\Xi^0(1620)$ pole satisfying Eq. (37) and the

TABLE VI. Scattering lengths a_0 and the pole positions of Model 1 and Model 2.

	a_0 (fm)	$\lvert a_0\rvert$ (fm)	z_{th} (MeV)	z estimated by Eq. (36) (MeV)
Model 1	0.80–0.92i	1.21	1607–29i [bbtttt]	1615–38i [bbtttt]
Model 2	−0.27–0.40i	0.48	1725+76i [ttbttt]	1701+228i [ttbttt]

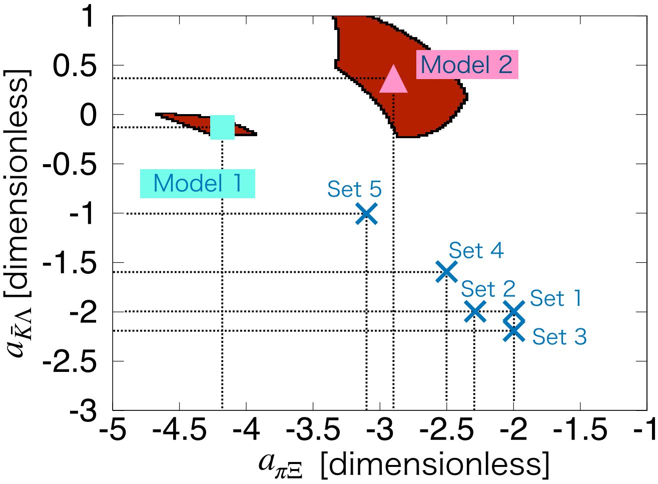

FIG. 11. Comparison of the parameter regions of the models with Eq. (37) and those with Eq. (38) in the $a_{\pi\Xi}$-$a_{\bar{K}\Lambda}$ plane. Triangle, square, and circle denote the parameters of Model 2, Model 1, and models in Ref. [12].

region with the $K^-\Lambda$ scattering length satisfying Eq. (38). For comparison, we also plot the subtraction constants of Sets 1–5 in Ref. [12]. We find that there is no solution which satisfies both the pole position in Eq. (37) and the $K^-\Lambda$ scattering length in Eq. (38). Based on the analysis in Sec. III and the results in Sec. IV C, we expect that this discrepancy is rooted to the nature of the quasibound state (*QB*) pole in Eq. (37) and the sign of the real and imaginary parts of the scattering length in Eq. (38). We also note that the Belle result (26) is obtained from the fit to the experimental $\pi\Xi$ spectrum by the Breit-Wigner distribution. For more quantitative comparison, it is necessary to perform the fit to the $\pi\Sigma$ spectrum directly, rather than the assumption of the pole position as in Eq. (37).

V. SUMMARY

In this work, focusing on Ξ(1620) for which new experimental constraints are available, we study the nature of the near-threshold state and the scattering length using numerical calculations with the chiral unitary approach. In Sec. III, we discuss the eigenstate represented by the near-threshold pole in the complex energy plane from the viewpoint of the scattering length in a two-channel problem. We show that the resonance above the threshold *R* and the quasibound state below the threshold *QB* are not directly connected due to the structure of the Riemann sheets, and in between *R* and *QB* there is a pole on the [tb] sheet which can be called the quasivirtual state *QV*. We show that the pole representing *QB*, *QV*, and *R* can be classified by the sign of the real and imaginary parts of the scattering length. In particular, the resonance *R* above the threshold cannot be expressed by only the scattering length, and the contribution from the effective range is necessary.

In Sec. IV A, we constructed Model 1 which reproduces the pole of the Ξ(1620) quasibound state as indicated by the Belle result. It is found that the imaginary part of the $\pi^+\Xi^-$ scattering amplitude shows a peak of Ξ(1620) in Model 1. At the same time, the threshold effect is quantitatively demonstrated through a comparison with the Breit-Wigner amplitude which has a pole at the same position.

Model 2 is constructed in Sec. IV B by reproducing the $K^-\Lambda$ scattering length by the ALICE experiment. We find that the $K^-\Lambda$ scattering amplitude shows a cusp structure at the threshold in Model 2. The pole of Ξ(1620) is not in the physically relevant Riemann sheet, but in the [ttbttt] sheet as a quasivirtual state.

In Sec. IV C, we estimate the pole positions from the $K^-\Lambda$ scattering lengths of Model 1 and Model 2 as an application of the discussion in Sec. III. As a result, we find that the estimated pole appears in the same Riemann sheet with the exact pole for both Model 1 and Model 2. Quantitatively, the pole is estimated with 10 MeV precision for Model 1, where the absolute value of the scattering length is of the order of 1 fm, while Model 2 with a smaller magnitude of the scattering length shows a deviation of about 150 MeV. We also discuss the near-threshold quasibound (*QB*) state in relation to the ALICE scattering length. We expect that the near-threshold *QB* states have a scattering length with large absolute value and positive real part. On the other hand, because the ALICE scattering length has small absolute value and negative real part, it is difficult to have a near-threshold *QB* state for the scattering amplitude with the ALICE constraint as long as the effects from the higher order are negligible.

In Sec. IV D, we examine the compatibility of the assumption of the quasibound Ξ(1620) state in Model 1 and the $K^-\Lambda$ scattering length using the ALICE measurement in Model 2 including the experimental uncertainties. At the same time, it should be kept in mind that the Belle data do not directly constrain the pole position of the scattering amplitude, and the near-threshold pole should be determined together with the threshold effect as shown in this paper.

As a future prospect, the calculation of the $\pi^+\Xi^-$ invariant mass spectrum in the $\Xi_c \to \pi^+\pi^+\Xi^-$ decay, as was done in Ref. [34], is important for comparison with the Belle data. This may provide a description of the Belle data in a way that is consistent with the ALICE measurement of the $K^-\Lambda$ scattering length. In this paper, we have discussed the $\bar{K}\Lambda$ threshold effect on the Ξ(1620) state. A similar threshold effect is expected for Ξ(1690) whose peak is located near the $\bar{K}\Sigma$ threshold at 1686.1 MeV. In this case, the threshold effect should be much more complicated because there are two thresholds ($K^-\Sigma^+$ and $\bar{K}^0\Sigma^0$ for the neutral channel) due to the isospin symmetry breaking. It is also important to investigate the internal structure of Ξ(1620) based on the models constructed in this paper. The internal structure can be extracted, for instance, by the method of the natural renormalization scheme in Ref. [35] and by the evaluation of the compositeness through the residue of the resonance pole [36,37].

ACKNOWLEDGMENTS

The authors thank Wren Yamada for useful discussion on Riemann sheets and the pole of the coupled-channel scattering. This work was supported in part by Grants-in-Aid for Scientific Research from JSPS (Grants No. JP22K03637, No. JP19H05150, and No. JP18H05402). This work was supported by JST, the establishment of university fellowships towards the creation of science technology innovation, Grant No. JPMJFS2139.

---

[1] R. L. Workman *et al.* (Particle Data Group), Review of particle physics, Prog. Theor. Exp. Phys. **2022**, 083C01 (2022).

[2] T. Hyodo and M. Niiyama, QCD and the strange baryon spectrum, Prog. Part. Nucl. Phys. **120**, 103868 (2021).

[3] M. Sumihama *et al.* (Belle Collaboration), Observation of $\Xi(1620)^0$ and evidence for $\Xi(1690)^0$ in $\Xi_c^+ \to \Xi^-\pi^+\pi^+$ decays, Phys. Rev. Lett. **122**, 072501 (2019).

[4] R. Aaij *et al.* (LHCb Collaboration), Evidence of a $J/\psi\Lambda$ structure and observation of excited Ξ^- states in the $\Xi_b^- \to J/\psi\Lambda K^-$ decay, Sci. Bull. **66**, 1278 (2021).

[5] S. Acharya *et al.* (ALICE Collaboration), ΛK femtoscopy in Pb-Pb collisions at $\sqrt{s_{NN}} = 2.76$ TeV, Phys. Rev. C **103**, 055201 (2021).

[6] N. Isgur and G. Karl, *P*-wave baryons in the quark model, Phys. Rev. D **18**, 4187 (1978).

[7] G. P. Engel, C. B. Lang, D. Mohler, and A. Schäfer (BGR), QCD with two light dynamical chirally improved quarks: baryons, Phys. Rev. D **87**, 074504 (2013).

[8] N. Kaiser, P. B. Siegel, and W. Weise, Chiral dynamics and the low-energy kaon-nucleon interaction, Nucl. Phys. A **594**, 325 (1995).

[9] E. Oset and A. Ramos, Non-perturbative chiral approach to S-wave KN interactions, Nucl. Phys. A **635**, 99 (1998).

[10] J. A. Oller and U. G. Meissner, Chiral dynamics in the presence of bound states: Kaon nucleon interactions revisited, Phys. Lett. B **500**, 263 (2001).

[11] T. Hyodo and D. Jido, The nature of the Λ(1405) resonance in chiral dynamics, Prog. Part. Nucl. Phys. **67**, 55 (2012).

[12] A. Ramos, E. Oset, and C. Bennhold, On the spin, parity and nature of the Ξ(1620) resonance, Phys. Rev. Lett. **89**, 252001 (2002).

[13] C. García-Recio, M. F. M. Lutz, and J. Nieves, Quark mass dependence of s-wave baryon resonances, Phys. Lett. B **582**, 49 (2004).

[14] D. Gamermann, C. Garcia-Recio, J. Nieves, and L. L. Salcedo, Odd parity light baryon resonances, Phys. Rev. D **84**, 056017 (2011).

[15] K. P. Khemchandani, A. Martínez Torres, A. Hosaka, H. Nagahiro, F. S. Navarra, and M. Nielsen, Why Ξ(1690) and Ξ(2120) are so narrow, Phys. Rev. D **97**, 034005 (2018).

[16] T. Sekihara, Ξ(1690) as a $\bar{K}\Sigma$ molecular state, Prog. Theor. Exp. Phys. **2015**, 091D01 (2015).

[17] K. Abe *et al.* (Belle), Observation of Cabibbo suppressed and *W*-exchange Λ_c^+ baryon decays, Phys. Lett. B **524**, 33 (2002).

[18] A. Feijoo, V. Valcarce Cadenas, and V. K. Magas, The Ξ(1620) and Ξ(1690) molecular states from $S = -2$ meson-baryon interaction up to next-to-leading order, Phys. Lett. B **841**, 137927 (2023).

[19] Y. I. Azimov, R. A. Arndt, I. I. Strakovsky, and R. L. Workman, Light baryon resonances: Restrictions and perspectives, Phys. Rev. C **68**, 045204 (2003).

[20] V. I. Kukulin, V. M. Krasnopol'sky, and J. Horacek, *Theory of Resonances* (Kluwer Academic, Dordrecht, 1989).

[21] N. Moiseyev, *Non-Hermitian Quantum Mechanics* (Cambridge University Press, Cambridge, 2011).

[22] T. Nishibuchi and T. Hyodo, Nature of excited Ξ baryons with threshold effects, EPJ Web Conf. **271**, 10002 (2022).

[23] Y. Ikeda, T. Hyodo, and W. Weise, Improved constraints on chiral SU(3) dynamics from kaonic hydrogen, Phys. Lett. B **706**, 63 (2011).

[24] Y. Ikeda, T. Hyodo, and W. Weise, Chiral SU(3) theory of antikaon-nucleon interactions with improved threshold constraints, Nucl. Phys. A **881**, 98 (2012).

[25] Z.-H. Guo and J. A. Oller, Meson-baryon reactions with strangeness −1 within a chiral framework, Phys. Rev. C **87**, 035202 (2013).

[26] D. Jido, E. Oset, and A. Ramos, Chiral dynamics of p wave in K^-p and coupled states, Phys. Rev. C **66**, 055203 (2002).

[27] D. Sadasivan, M. Mai, and M. Döring, *S*- and *p*-wave structure of $S = -1$ meson-baryon scattering in the resonance region, Phys. Lett. B **789**, 329 (2019).

[28] B. C. Pearce and B. F. Gibson, Observable effects of poles and shadow poles in coupled channel systems, Phys. Rev. C **40**, 902 (1989).

[29] W. A. Yamada, O. Morimatsu, T. Sato, and K. Yazaki, Near-threshold spectrum from a uniformized Mittag-Leffler expansion: Pole structure of the *Z*(3900), Phys. Rev. D **105**, 014034 (2022).

[30] R. J. Eden and J. R. Taylor, Poles and shadow poles in the many-channel *S* matrix, Phys. Rev. **133**, B1575 (1964).

[31] T. Hyodo, Structure of near-threshold *s*-wave resonances, Phys. Rev. Lett. **111**, 132002 (2013).

[32] T. Hyodo, Hadron mass scaling near the *s*-wave threshold, Phys. Rev. C **90**, 055208 (2014).

[33] C. Hanhart, J. R. Pelaez, and G. Rios, Remarks on pole trajectories for resonances, Phys. Lett. B **739**, 375 (2014).

[34] K. Miyahara, T. Hyodo, M. Oka, J. Nieves, and E. Oset, Theoretical study of the Ξ(1620) and Ξ(1690) resonances in $\Xi c \to \pi + MB$ decays, Phys. Rev. C **95**, 035212 (2017).

[35] T. Hyodo, D. Jido, and A. Hosaka, Origin of the resonances in the chiral unitary approach, Phys. Rev. C **78**, 025203 (2008).

[36] T. Hyodo, D. Jido, and A. Hosaka, Compositeness of dynamically generated states in a chiral unitary approach, Phys. Rev. C **85**, 015201 (2012).

[37] T. Sekihara, T. Hyodo, and D. Jido, Comprehensive analysis of the wave function of a hadronic resonance and its compositeness, Prog. Theor. Exp. Phys. **2015**, 063D04 (2015).